Journal of Combinatorial Mathematics and Combinatorial Computing
www.combinatorialpress.com/jcmcc

Combinatorial Press

Research on Multi-dimensional Dynamic Data Fusion and Real-time Calculation Method for Intelligent Monitoring of Safety Belts in Power Grid Construction Environment

Xuxin Li[1,✉], Shishuo Chen[1], Xiaoyun Tang[1], Yuhang Qiu[1], Zhiping Ke[1]

[1] *Chaozhou Power Supply Bureau Guangdong Power Grid Co., Ltd, Chaozhou, Guangdong, 521000, China*

ABSTRACT

This paper proposes a real-time computational method for multidimensional dynamic data fusion (VIO-SLAM) for intelligent monitoring of seat belts in the grid construction environment. In this paper, the optical flow method is first used to process and track point features, and the geometrically constrained line matching algorithm is utilized to improve the accuracy of feature matching. Combined with IMU modeling and pre-integration techniques, it effectively reduces the computation of high-frequency IMU data and improves the system efficiency. At the same time, a real-time lightweight semantic segmentation system is constructed to achieve fast semantic understanding of the construction scene. The real-time and accuracy of data processing is further improved by sliding window method with BA optimization. On this basis, a VIO-SLAM algorithm based on EKF fusion of multidimensional dynamic data is proposed to realize real-time monitoring and localization of seat belt status. The results show that when a dangerous collision occurs in a complex power grid construction environment, the protection performance of shoulder belt, neck bending moment force and head acceleration of the construction personnel under the method of this paper is much higher than that of the traditional seat belt. In the process of emergency collision avoidance, the VIO-SLAM algorithm is able to tighten the seat belt in advance for the construction personnel, which has better protection performance and can achieve the purpose of "collision avoidance and damage reduction". The pre-tensioning force for eliminating the gap in the webbing of seat belts and the pre-tensioning force for somatosensory warning reminders are also determined to improve the protection performance of construction workers.

Keywords: VIO-SLAM, Optical flow method, IMU pre-integration, Real-time lightweight semantic segmentation, EKF fusion method, Intelligent monitoring of seat belts

✉ Corresponding author.
E-mail address: jkyt2009@163.com (X. Li).
Received 25 February 2024; Revised 10 May 2024; Accepted 15 December 2024; Published Online 15 April 2025.
DOI: 10.61091/jcmcc127a-421

1. Introduction

Smart grid is both the direction of power grid development and one of the hot research areas at present and for quite some time to come [1-2]. Smart grid fully applies the technologies of measurement and perception, data mining, simulation and analysis, automatic control, information communication, power electronics, intelligent decision-making, etc., to the grid, transforming the rigid traditional grid into a new type of grid that is self-perceiving, self-recovering, green, efficient, and friendly and interactive, so as to significantly enhance the degree of intelligence of the power system [3-6]. Its research covers many aspects of the power system, such as generation, transmission, transformation, distribution, utilization, and scheduling [7].

As a large number of businesses and organizations have shifted to the home office model, there has been an unprecedented change in electricity demand, with a decrease in traditional commercial and industrial electricity demand and a significant increase in electricity consumption by residential households [8-9]. This change in demand has forced the electric power industry to change its approach to human resource deployment and execution of field operations [10-11]. In order to guarantee the power supply and ensure the normal operation of residents' life and production, power grid personnel need to run around more in the front-line field operations to ensure the stability and safety of the operation of power equipment [12-13]. They need to monitor the operation of power facilities at all times, find and solve potential problems in time, and ensure the continuity and reliability of the power supply system [14-15]. In the face of various emergencies, they need to respond quickly, take effective measures to restore power supply, and carry out restoration and maintenance work quickly in emergency situations to minimize power outage time and safeguard users' power needs [16-17]. In the face of irregular and unauthorized operation in the grid scene operation, strengthening the safety monitoring of the grid scene can effectively reduce the risk of accidents [18-19]. The application of intelligent safety monitoring technology in the grid scene has become the key, and by introducing some advanced models of deep learning, intelligent safety monitoring can be realized to discover the irregular and illegal operations and abnormalities in the grid scene in a timely manner and take corresponding measures to guarantee the stable operation of the power system and ensure the normal operation of the residents' life and production [20-21]. Under the form of the continuous promotion of China's smart grid construction, the requirements of electric power enterprises for safe operation are becoming more and more stringent, and at the same time, with the increasing maturity of the Internet of Things (IoT) technology, the cost of IoT-related hardware and software is also decreasing. Therefore, the research direction of substation operation safety monitoring with the help of IoT technology not only has a wide range of practical needs, but also has a complete technical basis and cost advantages, and its application prospect is very broad [22-24].

In this paper, we utilize the optical flow method for real-time processing and tracking of key point features of seat belts, combined with geometrically constrained line matching algorithms, to improve the tracking accuracy of the feature points of seat belt images in the intelligent monitoring environment. Through IUM modeling and pre-integration techniques, the redundant computation of high-frequency IMU data is effectively reduced to improve the real-time performance of the intelligent monitoring system. In addition, a lightweight real-time semantic segmentation system is designed in this paper, which is able to quickly recognize the dangerous areas and key equipment in the construction site and provide semantic support for the dynamic monitoring of safety belts. The accuracy and stability of real-time data computation are further improved by sliding window method and BA optimization. A VIO-SLAM algorithm based on Extended Kalman Filter (EKF) fusion of multidimensional dynamic data is proposed to fuse the positional data to obtain more accurate results and realize the real-time positional condition monitoring of safety belts. Finally, the effectiveness and reliability of this paper's method in complex environments are verified through testing in actual grid construction scenarios, providing technical support for power construction safety management.

2. Intelligent safety belt monitoring technology for power grid construction based on VIO-SLAM

2.1. Pre-processing of grid construction environment data based on point and line features

2.1.1. Point feature processing tracking algorithm based on the optical flow method. Optical flow [25] is a method for describing the motion of pixels between images over time, essentially estimating the motion of pixels between images at different moments, with the goal of solving for where the pixel has arrived at the next moment.

Let the gray value of the pixel located at the image coordinate system (x, y) at the moment t be $I(x, y, t)$. After time Δt, the pixel moves to $(x+dx, y+dy)$ and its gray value is $I(x+dx, y+dy, t+dt)$, which can be obtained according to the assumption of gray invariance:

$$I(x+dx, y+dy, t+dt) = I(x, y, t) \tag{1}$$

A first-order Taylor expansion to the left of the equal sign yields:

$$I(x+dx, y+dy, t+dt) \approx I(x, y, t) + \frac{\partial I}{\partial x}dx + \frac{\partial I}{\partial y}dy + \frac{\partial I}{\partial t}dt \tag{2}$$

Since the gray scale is unchanged:

$$\frac{\partial I}{\partial x}dx + \frac{\partial I}{\partial y}dy + \frac{\partial I}{\partial t}dt = 0 \tag{3}$$

Divide both sides by dt at the same time to get:

$$\frac{\partial I}{\partial x}\frac{dx}{dt} + \frac{\partial I}{\partial y}\frac{dy}{dt} = -\frac{\partial I}{\partial t} \tag{4}$$

where $\partial I/\partial x$ and $\partial I/\partial y$ denote the gradient of the image in the x, y direction I_x and I_y, respectively, dx/dt and dy/dt denote the velocity of the pixel in the x, y direction u, v, $\partial I/\partial t$ is the change of the image grayscale with respect to time I_t. The function of the image grayscale with respect to time I_t is:

$$I_x u + I_y v = -I_t \tag{5}$$

Assuming that a window of size $w \times w$ contains w^2 pixels and each pixel has the same motion, there:

$$I_x u + I_y v = -I_{tk}, k = 1, \ldots, w^2 \tag{6}$$

The least squares solution to the above equation gives the pixel movement speed u, v:

$$\begin{bmatrix} u \\ v \end{bmatrix}^* = -(A^T A)^{-1} A^T b \tag{7}$$

Of these, $A = \begin{bmatrix} [I_x, I_y]_1 \\ \ldots \\ [I_x, I_y]_k \end{bmatrix}, b = \begin{bmatrix} I_{t1} \\ \ldots \\ I_{tk} \end{bmatrix}$.

2.1.2. Line matching algorithm based on geometric constraints. In this paper, geometric constraints between point features and line features are utilized to improve the real-time performance of the system, and the method can greatly reduce the time consumption of line matching.

The line segments that meet the conditions for line matching are selected based on the results of adding feature points to the line segments, the number of feature points on the line segments must not be less than two, in order to increase the number of eligible lines, the points whose distances from the line segments are less than a set threshold are still regarded as being on the line segments, and all eligible line segments finally form line feature set L_{c_i}, and the points on line segment $l_k \in L_{c_i}$ belong to set $P_{ci\_l_k}$. Tracking the line segments between consecutive image frames $c_i - 1$ and c_i, that is, from L_{ci-1} to L_{c_i}, and between line segments $l_1(s_1, e_1) \in L_{c_{i-1}}$ and $l_2(s_2, e_2) \in L_{c_i}$ must satisfy the following three conditions for a successful match:

Condition 1: $P_{c_{i-1}\_l_1}$ and $P_{c_i\_l_2}$ have at least two feature points.

Condition 2: The length $\| l_2 \|$ of l_2 should be similar to the length $\| l_1 \|$ of l_1, and l_1, l_2 should satisfy the following relation:

$$\frac{\max(\| l_1 \|, \| l_2 \|)}{\min(\| l_1 \|, \| l_2 \|)} < T_l \in \square \tag{8}$$

Condition 3: Assuming that l_1, l_2 is in the same direction, the distance d between the l_1, l_2 endpoints should satisfy the following equation:

$$d_{s_1 s_2} < T_d, d_{e_1 e_2} < T_d \tag{9}$$

1) Plücker line coordinates. where T_l, T_d is set to 150 and 100 pixels, respectively, and feature matching between consecutive image frames can be accomplished by the above steps.

In this paper, two parametric forms are used to represent lines, firstly, the plücker line coordinates [26] are used to reconstruct the newly observed line features in 3D space, and then they are minimized by iteratively updating the minimum four-parameter standard orthogonal representations of the plücker coordinates, which makes the representation of the lines in 3D space more compact and computationally simpler.

2) Plücker line coordinates. A 3D spatial line L in plücker coordinates is denoted as $L = (n^T, d^T)^T \in R^6$, where $d \in R^3$ is the direction vector of the line, $n \in R^3$ is the normal vector of the plane defined by the line and the coordinate origin, and the relationship between n and d is $n^T d = 0$. The transformation matrix T_{cw} of a given line segment from the world coordinate system w to the camera coordinate system c is:

$$T_{cw} = \begin{bmatrix} R_{cw} & p_{cw} \\ 0 & 1 \end{bmatrix} \tag{10}$$

Transform the plücker coordinates of the line by the above equation:

$$L^c = \begin{bmatrix} n^c \\ d^c \end{bmatrix} = T_{cw} L_{cw} = \begin{bmatrix} R_{cw} & [p_{cw}]_\times R_{cw} \\ 0 & R_{cw} \end{bmatrix} L^w \tag{11}$$

where $[\cdot]_x$ is the skew-symmetric matrix of 3D vectors.

When a new road marking line is observed in two different camera views, it is easy to compute the plücker coordinates of this line. A 3D spatial straight line L is captured in both consecutive image frames c_1 and c_2, a straight line L is represented as $z_L^{c_1}, z_L^{c_2}$ in image frames c_1 and c_2, respectively, and the two endpoints of the line segment $z_L^{c_1}$ in the normalized image plane are represented as $s^{c_1} = [u_s, v_s, 1]^T, e^{c_1} = [u_e, v_e, 1]^T$, which satisfy the following equation for the plane $\pi = \left[\pi_x, \pi_y, \pi_z, \pi_w\right]^T$ determined in 3D space with the coordinate origin $C = [x_0, y_0, z_0]^T$:

$$\pi_x(x-x_0)+\pi_y(y-y_0)+\pi_z(z-z_0)=0 \tag{12}$$

where $[\pi_x,\pi_y,\pi_z]^T=[s^{c_1}]_x e^{c_1},\pi_w=\pi_x x_0+\pi_y y_0+\pi_z z_0$. The c_1 planes π_1 and π_2 in the given image frame 2 and the pairwise plücker matrix L^* is:

$$L^*=\begin{bmatrix}[d]_\times & n \\ -n^T & 0\end{bmatrix}=\pi_1\pi_2^{\ T}-\pi_2\pi_1^{\ T}\in R^{4\times4} \tag{13}$$

3) Orthogonal representation. The 3D spatial line has four degrees of freedom, and the standard orthogonal representation $(U,W)\in SO(3)\times SO(2)$ is more appropriate than the plücker coordinates in the optimization process, and the fact that the two are interconvertible means that they can be employed for different purposes in a SLAM system. A coordinate system is defined on the 3D spatial line, where the two axes of the coordinate system are the normal and direction vectors of the normalization plane, and then a third axis is determined from these two axis vectors. Define the rotation matrix U between the line coordinates and the camera coordinate system as:

$$U=R(\psi)=\left[\frac{n}{\|n\|},\frac{d}{\|d\|},\frac{n\times d}{\|n\times d\|}\right] \tag{14}$$

where $\psi=[\psi_1,\psi_2,\psi_3]^T$ consists of the angle of rotation around the x,y,z -axis of the camera coordinate system.

The plücker coordinates are related to U by:

$$[n,d]=\left[\frac{n}{\|n\|},\frac{d}{\|d\|},\frac{n\times d}{\|n\times d\|}\right]\begin{bmatrix}\|n\| & 0 \\ 0 & \|d\| \\ 0 & 0\end{bmatrix} \tag{15}$$

Expressed in terms of trigonometric functions:

$$W=\begin{bmatrix}\cos(\phi) & -\sin(\phi) \\ \sin(\phi) & \cos(\phi)\end{bmatrix}=\frac{1}{\sqrt{(\|n\|^2+\|d\|^2)}}\begin{bmatrix}\|n\| & -\|d\| \\ \|d\| & \|n\|\end{bmatrix} \tag{16}$$

where ϕ is the rotation angle. W contains information about the distance from the coordinate origin to the 3D straight line $d=\|n\|/\|d\|$, which is defined according to U and W, which include three degrees of freedom for the rotation matrix and one degree of freedom for the distance d, and is optimized using $O=[\psi,\phi]^T$ as the minimum representation of the 3D spatial line. The 3D space line L optimized with the standard orthogonal representation corresponds to the plücker coordinates:

$$L=[w_1u_1^T,w_2u_2^T]^T=\frac{1}{\sqrt{(\|n\|^2+\|d\|^2)}}L \tag{17}$$

where u_i is the ird column of matrix U, $w_1=\cos(\phi),w_2=\sin(\phi)$. L and L represent the same 3D spatial line, although there is a scale factor between them.

2.1.3. IMU modeling. The inertial navigation system is mainly divided into an error model and a kinematic model, and Gaussian white noise and random wander error are mainly considered in the error model, which can be obtained by IMU calibration [27]. The six-axis IMU sensor consists of a three-axis accelerometer and a three-axis gyroscope, which are used to measure the acceleration a and the angular velocity ω at discrete moments, respectively.The measurements $\hat{\omega},\hat{a}$ of the IMU raw gyroscope and accelerometer are affected by the IMU bias error and the Gaussian white noise, which both belong to the random error.

Under the influence of bias and white noise, the gyroscope and accelerometer measurements of the IMU in the body coordinate system are respectively:

$$\hat{\omega} = \omega^b + b_g^b + n_g^b \tag{18}$$

$$\hat{a} = R_{bw}(a^w + g^w) + b_a^b + n_a^b \tag{19}$$

The above equation is the error model of the inertial navigation system. Where, b denotes the body coordinate system body of IMU, b_g^b, b_a^b is the bias error of gyroscope and accelerometer respectively, n_g^b, n_a^b is the white noise of gyroscope and accelerometer, R_{bw} denotes the transformed quaternion from the world coordinate system w to the body coordinate system, $g^w = [0,0,g]^T$ is the gravity vector in the world coordinate system, and ω^b, a^w is the true value in the IMU coordinate system and the world coordinate system respectively.

n_g^b and n_a^b obey Gaussian distributions as follows:

$$n_g^b \sim \mathrm{N}\,(0, \sigma_g{}^2), n_a^b \sim \mathrm{N}\,(0, \sigma_a{}^2) \tag{20}$$

The derivatives of b_g^b and b_a^b also follow a Gaussian distribution:

$$\dot{b}_g^b \sim \mathrm{N}\,(0, \sigma_{b_g}{}^2), \dot{b}_a^b \sim \mathrm{N}\,(0, \sigma_{b_a}{}^2) \tag{21}$$

In the time-continuous case, the dynamics of the IMU drive system is formulated as follows:

$$\dot{p}_{wb_t} = v_t^w, \dot{v}_t^w = a_t^w, \dot{q}_{wb_t} = q_{wb_t} \otimes \begin{bmatrix} 0 \\ \frac{1}{2}\omega^{b_t} \end{bmatrix} \tag{22}$$

where $\otimes$ denotes the quaternion multiplication operation.

Knowing the state of the IMU at the moment of $t = i$: $p_{wb_i}, v_i^w, q_{wb_i}$ and the continuous value of w, a in time $t \in [i, j]$, the state of the IMU at the moment of $t = j$ can be obtained by integrating the IMU measurements, i.e., the model of the IMU motion at continuous time $t \in [i, j]$:

$$\begin{cases} p_{wb_j} = p_{wb_i} + v_i^w \Delta t + \iint_{t\in[i,j]} (R_{wb_t} a^{b_t} - g^w)\delta t^2 \\ v_j^w = v_i^w + \int_{t\in[i,j]} (R_{wb_t} a^{b_t} - g^w)\delta t \\ q_{wb_j} = \int_{t\in[i,j]} q_{wb_t} \otimes \left[\frac{1}{2}\omega^{b_t}\right]\delta t \end{cases} \tag{23}$$

where Δt is the time difference between i and j.

2.1.4. IMU pre-integration. The processing of the IMU pre-integration focuses on the calculated value of the IMU between the two image frames and the amount it is updated each time, deriving the measured value of the change in PVQ (position, velocity, attitude) during this period and comparing it with the estimation of the motion through vision, obtaining the residual value, and from this constructing a cost function for the PVV values for optimization.

The IMU can measure its own angular velocity and acceleration, from which the IMU observation model can be derived:

$$\tilde{\omega}^b = \omega^b + b^g + n^g \tag{24}$$

$$\tilde{a}^b = q_{bw}(a^w + g^w) + b^a + n^a \tag{25}$$

where $\tilde{\omega}^b$ and $\tilde{a}^b$ are the observed values of gyroscopes and accelerometers respectively, ω^b and a^w denote the true values, b^g and b^a are the zero bias of gyroscopes and accelerometers respectively, n^g and n^a are their observation noise respectively, the right superscript b means the IMU coordinate system and the right superscript w means the world coordinate system.

The derivative of PVQ with respect to time is:

$$\begin{aligned} \dot{p}_{wb_t} &= v_t^w \\ \dot{v}_t^w &= a_t^w \\ \dot{q}_{wb_t} &= q_{wb_t} \otimes \begin{bmatrix} 0 \\ \frac{1}{2}\omega^{b_t} \end{bmatrix} \end{aligned} \tag{26}$$

Integrating the measurements from moment i to moment j yields j moment PVQ, denoted:

$$\begin{aligned} p_{wb_j} &= p_{wb_i} + v_i^w \Delta t + \iint_{t\in[i,j]} (q_{wb_t} a^{b_t} - g^w)\delta t^2 \\ v_j^w &= v_i^w + \int_{t\in[i,j]} (q_{wb_t} a^{b_t} - g^w)\delta t \\ q_{wb_j} &= \int_{t\in[i,j]} q_{wb_t} \otimes \begin{bmatrix} 0 \\ \frac{1}{2}\omega^{b_t} \end{bmatrix} \delta t \end{aligned} \tag{27}$$

In the process of BA optimization, all q_{wb_t} updates need to be re-integrated according to the above equation, which is computationally intensive, and this is the problem mentioned in this subsection. This can be transformed into an integral model by transforming the integral term in the above equation from a pose relative to the world coordinate system to a relative i moment. The j-moment PVQ is then noted as:

$$\begin{aligned} p_{wb_j} &= p_{wb_i} + v_i^w \Delta t - \frac{1}{2} g^w \Delta t^2 + q_{wb_i} \iint_{t\in[i,j]} (q_{b_i b_t} a^{b_t})\delta t^2 \\ v_j^w &= v_i^w - g^w \Delta t + q_{wb_i} \int_{t\in[i,j]} (q_{b_i b_t} a^{b_t})\delta t \\ q_{wb_j} &= q_{wb_i} \int_{t\in[i,j]} q_{b_i b_t} \otimes \begin{bmatrix} \frac{1}{2}\omega^{b_t} \end{bmatrix} \delta t \end{aligned} \tag{28}$$

For the partial terms in the above equation, defined as pre-integrated quantities, they are related only to the measured values and are the values of the direct integration of the IMU data from moment i to moment j, the pre-integrated quantities are:

$$\begin{aligned} \alpha_{b_i b_j} &= \iint_{t\in[i,j]} (q_{b_i b_t} a^{b_t})\delta t^2 \\ \beta_{b_i b_j} &= \int_{t\in[i,j]} (q_{b_i b_t} a^{b_t})\delta t \\ q_{b_i b_j} &= \int_{t\in[i,j]} q_{b_i b_t} \otimes \begin{bmatrix} 0 \\ \frac{1}{2}\omega^{b_t} \end{bmatrix} \delta t \end{aligned} \tag{29}$$

The following equation is obtained by first substituting the pre-integrated quantity into Eq. (27) and adding the zero bias to organize it:

$$\begin{bmatrix} p_{wb_j} \\ v_j^w \\ q_{wb_j} \\ b_j^a \\ b_j^g \end{bmatrix} = \begin{bmatrix} p_{wb_i} + v_i^w \Delta t - \frac{1}{2} g^w \Delta t^2 + q_{wb_i} \alpha_{b_i b_j} \\ v_i^w - g^w \Delta t + q_{wb_i} \beta_{b_i b_j} \\ q_{wb_i} q_{b_i b_j} \\ b_i^a \\ b_i^g \end{bmatrix} \tag{30}$$

The pre-integrated quantity of the IMU between moments i and j is taken as a measurement, and the state quantity is constrained to obtain the pre-integrated error:

$$r_b(Z_{b_i b_{i+1}}, X) = \begin{bmatrix} r_p \\ r_v \\ r_q \\ r_{ba} \\ r_{bg} \end{bmatrix} = \begin{bmatrix} q_{b_i w}\left(p_{wb_j} - p_{wb_i} - v_i^w \Delta t + \frac{1}{2} g^w \Delta t^2 \right) - \alpha_{b_i b_j} \\ q_{b_i w}(v_j^w - v_i^w + g^w \Delta t) - \beta_{b_i b_j} \\ 2\left[q_{b_j b_i} \otimes (q_{b_i w} \otimes q_{wb_j}) \right]_{xyz} \\ b_j^a - b_i^a \\ b_j^g - b_i^g \end{bmatrix} \tag{31}$$

where $X = [p_{wb_i}, v_i^w, q_{wb_i}^a, b_{b_i}^g, b_{b_i}^w, p_{wb_j}^a, v_j^w, q_{wb_j}^a, b_{b_j}^g]$, $[\cdot]_{xyz}$ means to take only the three-dimensional vectors composed of quaternionic imaginary parts. Now we get the IMU residuals from moment i to moment j then the optimization function constructed in the IMU part of BA is:

$$\sum_{i \in B} \rho(\| r_b(Z_{b_i b_{i+1}}, X) \|^2_{\Sigma_{b_i b_{i+1}}}) \tag{32}$$

2.2. Model of real-time lightweight semantic segmentation system

In order to improve the real-time performance of the semantic system for intelligent monitoring based on the effective processing of images of the grid construction environment, this paper proposes a real-time semantic computing SLAM method based on dynamic probabilistic optimization of intelligent monitoring based on the real-time semantics of the dynamic scene localization of the safety belt intelligent monitoring [28] system in the grid construction environment as the main framework on the basis of the previous research. It is applicable to lightweight segmentation models for continuous images and applied to the SLAM system for intelligent monitoring of power grid construction environment to provide real-time semantic information for the system.

2.2.1. System framework. The overall system box is shown in Fig. 1. In this paper, the tracking thread in the grid construction environment is partially modified, and some criteria are appropriately lowered when keyframes are selected to produce a larger number of keyframes than SLAM, to ensure the number of keyframes required by the overall system for the subsequent screening of static semantic keyframes. In addition, a new semantic segmentation thread is added in this paper, which can run in parallel with the tracking thread and local map building thread to improve the overall running speed of the intelligent monitoring system. The semantic segmentation thread only accepts keyframe images as input, and by segmenting the input intelligent surveillance seatbelt images and combining with the proposed static semantic keyframe selection method, the system can determine which keyframes belong to the static semantic keyframes. When the discriminative conditions are satisfied, the static semantic keyframe will be input to the local map building thread, while the semantic segmentation thread generates a binarized mask map based on its segmentation results, which is used to differentiate between dynamic and static regions, and assigns the corresponding dynamic probabilities to the feature points in the intelligent monitoring image of seat belts in the power grid construction environment.

Since the system only segments the key frames, in order to ensure the accuracy of the dynamic probability of the feature points in each input real-time monitoring image, this paper proposes a dynamic probability updating and propagation method based on the inter-frame feature point matching relationship and the matching relationship between the feature points and the points of the intelligent monitoring seatbelt image under the power grid construction environment, and ultimately completes the initial estimation of the camera's position by utilizing the screened static point pairs.

In the local BA stage, this paper combines the dynamic probability with the optimization process, using the dynamic probability of the intelligent monitoring seat belt image points to derive the corresponding BA optimization weights, and then using this to calculate the weighted reprojection error.

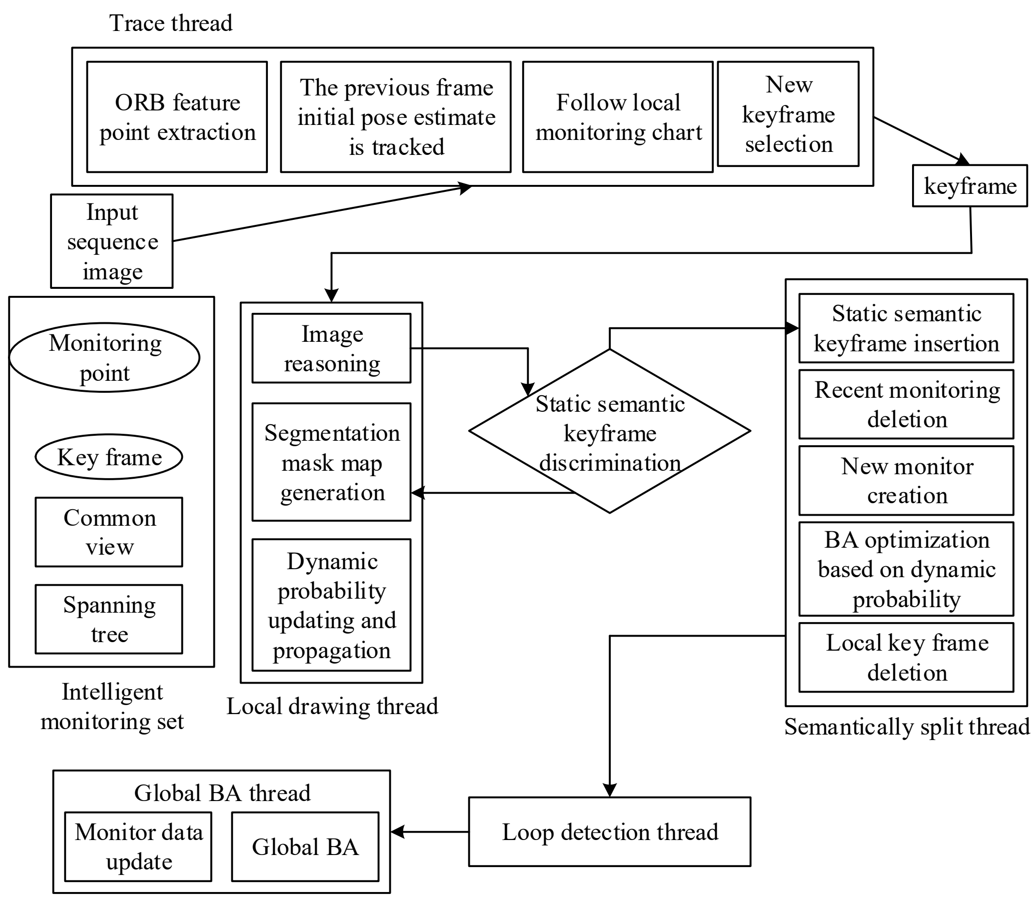

Fig. 1. Overall system diagram

2.2.2. Tracking threads. For the feature points extracted in the tracking process of intelligent monitoring seat belt in the grid construction environment, all of them are expressed in this paper by dynamic probability to indicate their dynamic degree, and combined with the results of semantic segmentation, the dynamic probability of real-time calculation of the feature points and their matching intelligent monitoring seat belt image points will be propagated and updated, in addition, the system will also be based on the segmentation results of the current keyframe to determine whether it meets the conditions of static semantic keyframe filtering.

1) Static semantic keyframe selection. In the dynamic scene of power grid construction, in order to let more static information in the key frames participate in the back-end optimization process, reduce the

influence of the dynamic intelligent monitoring seat belt image points, and improve the accuracy of the camera position optimization, this paper proposes a real-time computational static semantic key frame selection method based on the key frame selection strategy of SLAM, according to the semantic information within the seat belt image.

Assuming I_t is the keyframe selected by SLAM at the t moment, $I_{i.j}$ is the pixel point at the (i,j) position in the keyframe, and defining $S_{staitc}, S_{dynamic}$ variables for representing the static semantic score and dynamic semantic score of the current image.

After obtaining the key frame I_t to be processed, it is fed into the semantic segmentation thread to derive the segmentation result of this image. If the category of the region to which $I_{i,j}$ belongs is dynamic objects such as pedestrians and vehicles, $S_{dynamic}(i,j)$ is set to 1, otherwise it is 0. If the category of the region to which the pixel point belongs is high static objects such as buildings and traffic markers, $S_{static}(i,j)$ is assigned to 1, and if it is a low static object such as a seat or a grid display, $S_{static}(i,j)$ is 0.5.

Next, according to the static semantic score and dynamic semantic score within the image, determine whether the current keyframe can be used as a static semantic keyframe or not, the discriminative conditions are shown below:

$$score = \frac{\sum_{(i,j)\in I} S_{static}}{1+\sum_{(i,j)\in I} S_{dynamic}} \tag{33}$$

If the Score of the current frame exceeds the set threshold 3, it is determined to be a static semantic keyframe and inserted into the keyframe sequence to serve the subsequent workflow.

2) Dynamic probability initialization. Considering the limitations of the semantic segmentation model in the complex grid construction environment, this paper does not directly distinguish dynamic and static points based on the segmentation results of the current frame, but synthesizes the static semantic keyframes from multiple viewpoints of intelligent monitoring, and calculates and updates the dynamic probability of the 3D seatbelt image points in intelligent monitoring in real time.

Suppose that the static semantic keyframe selected at the current moment is I_1, the previous reference static semantic keyframe is marked as I_{i-1}, M_i is represented as the three-dimensional intelligent monitoring safety belt atlas points in the intelligent monitoring seat belt atlas that meet the matching relationship with I_i, I_{i-1}, the dynamic probability of M_i on the previous static semantic key is represented as $P_{i-1}(M_i)$, M_i is represented as $X_i(M_i)$ according to the current static semantic keyframe segmentation mask map, and the updated dynamic probability is expressed as $P_i(M_i)$. If the 2D projection points of M_i in the current static semantic keyframe are distributed within the mask region, it will be initially determined as a dynamic attribute, and $X_i(M_i)$ will be denoted as 1, otherwise 0. In this paper, the following formula is utilized to realize the dynamic probability real-time calculation and update:

$$P_t(M_i) = (1-\lambda)P_{t-1}(M_i) + \lambda X_t(M_i) \tag{34}$$

where λ is used as a parameter to balance the probability value of the previous moment with the observation value of the current moment, when λ is larger, it indicates that the updated dynamic probability value relies more on the observation value at the time of segmentation, and when λ is smaller, it represents that the probability value of the previous moment has a greater influence on the dynamic probability value of the current moment. Considering that the semantic segmentation model will occur segmentation error in some moments, this paper sets λ to 0.3.

2.2.3. BA. Taking BA in vision SLAM as an example, in this paper, two-frame image feature point matching is used to estimate the changes in camera position (R, t) during the shooting of seat belt pictures under intelligent monitoring in the grid construction environment, and the coordinates of the triangulation-reduced point P in the world coordinate system. For a number of observed and restored road marking points will become feature points in the real-time intelligent monitoring images taken by cameras with different positions, if the spatial position of these road marking points and camera positions are adjusted so that the light emitted from these road marking points can all point to the center of light of the cameras at each position, the process is BA, and the principle of BA is shown in Fig. 2.

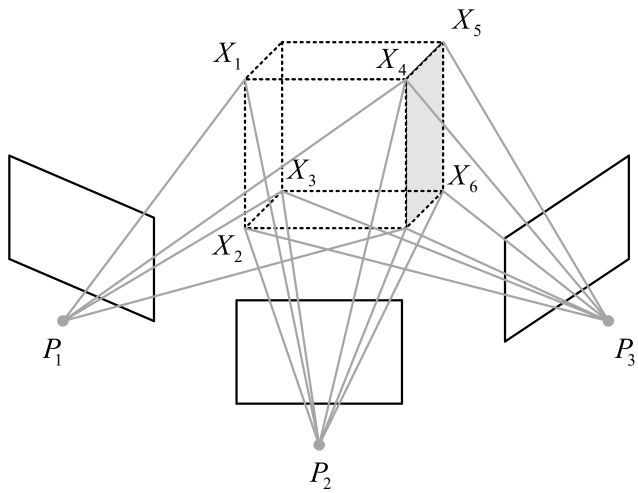

Fig. 2. The principle diagram of BA

At this point, first take a road marking point as an example, its coordinates in space is $[x, y, z]^T$, assuming that the road marking point is identified as a feature point, the observed value $[u, v]^T$ is in the camera normalized plane coordinates, then in the normalized plane estimate and the observed value error is recorded as:

$$r_c = \begin{bmatrix} \frac{x}{z} - u \\ \frac{y}{z} - v \end{bmatrix} \tag{35}$$

where $\lambda = 1/z$ is the inverse depth, the introduction of the inverse depth is because the optimization of the waypoints in the BA process consumes a lot of arithmetic, if the waypoints are far away then the error caused by the error will be very large, the cost function will be forced to make a larger adjustment, so the introduction of the inverse depth can effectively solve the problem. Namely:

$$\begin{bmatrix} x \\ y \\ z \end{bmatrix} = \frac{1}{\lambda} \begin{bmatrix} u \\ v \\ 1 \end{bmatrix} \tag{36}$$

If the waypoint is restored in frame i and observed in frame j, the point is predicted to be marked in frame j in the normalized camera coordinate system:

$$\begin{bmatrix} x_{c_j} \\ y_{c_j} \\ z_{c_j} \\ 1 \end{bmatrix} = T_{bc}^{-1} T_{wb_j}^{-1} T_{wb_i} T_{bc} \begin{bmatrix} \frac{1}{\lambda} u_{c_i} \\ \frac{1}{\lambda} v_{c_i} \\ \frac{1}{\lambda} \\ 1 \end{bmatrix} \tag{37}$$

The reprojection error of the point is:

$$r_c = \begin{bmatrix} \frac{x_{cj}}{z_{cj}} - u_{cj} \\ \frac{y_{cj}}{z_{cj}} - v_{cj} \end{bmatrix} \tag{38}$$

The above is for a waypoint in the residuals between two frames of the image, and in fact there are many waypoints and keyframes, which constitute many residuals between them, and these residuals constitute a cost function denoted as:

$$\sum_{(i,j)\in F} \rho\left(\| r_f(z_{f_j}^{c_i}, x) \|_{\Sigma_{f_j}^{c_i}}^2 \right) \tag{39}$$

where c_i means the ind camera coordinate system, $Z_{f_j}^{c_i}$ means the observation of c_i on f_j, and $X = [x_c, x_p]$ at this point is the set of bit positions and waypoints. The least squares solution of the above equation is performed to optimize each camera position and waypoint coordinates, which is BA.

Assuming that Eq. (39) is solved using Gaussian Newton method, the final problem is transformed into solving the incremental equations as follows:

$$\underbrace{J(x)J^T}_{H(x)}(x)\Delta x = \underbrace{-J(x)f(x)}_{g(x)} \tag{40}$$

$$H\Delta x = g \tag{41}$$

Suppose there are two bit poses and six waypoints for BA, whose H is structured in such a way that C_1, C_2 is the camera bit pose, $P_1, P_2, P_3, P_4, P_5, P_6$ is the waypoint, and C_1 can be observed as P_1, P_2, P_3, P_4, C_2 can be observed as P_3, P_4, P_5, P_6.

By dividing H into four pieces, each of which is B, E, E^T, C, Eq. (41) can be transformed into the following equation:

$$\begin{bmatrix} B & E \\ E^T & C \end{bmatrix} \begin{bmatrix} \Delta x_c \\ \Delta x_p \end{bmatrix} = \begin{bmatrix} v \\ w \end{bmatrix} \tag{42}$$

In order to eliminate the non-diagonal portion E in the upper right corner of Eq. (42) a transformation of Eq:

$$\begin{bmatrix} I & -EC^{-1} \\ 0 & I \end{bmatrix} \begin{bmatrix} B & E \\ E^T & C \end{bmatrix} \begin{bmatrix} \Delta x_c \\ \Delta x_p \end{bmatrix} = \begin{bmatrix} I & -EC^{-1} \\ 0 & I \end{bmatrix} \begin{bmatrix} v \\ w \end{bmatrix} \tag{43}$$

The collation yields the following equation:

$$\begin{bmatrix} B - EC^{-1}E^T & 0 \\ E^T & C \end{bmatrix} \begin{bmatrix} \Delta x_c \\ \Delta x_p \end{bmatrix} = \begin{bmatrix} v - EC^{-1}w \\ w \end{bmatrix} \tag{44}$$

From this, the first line of the equation is independent of Δx_p and can be solved for Δx_c before substituting Δx_c into the second line of the equation to find Δx_p. Where $B - EC^{-1}E^T$ is called the Schur complement of C with respect to H.

2.2.4. Sliding window method. A number of keyframes and waypoints will be BA for optimization, however, if we let the keyframes and waypoints keep accumulating, the residual terms will become more and more, which will generate a huge amount of computation. Therefore, in order to maintain the number of optimized variables in a reasonable range, the BA process can be controlled in a fixed-size window with the help of the sliding window method, which dynamically adds and removes the variables to be optimized.

For this window, the keyframes and waypoints of the new seatbelt smart surveillance images are added to compute the BA process in the same way as before, except that the variables to be optimized are increased, but directly removing the old keyframes and the corresponding waypoints will lead to loss of information and destroy the constraints. Therefore removing keyframes requires the use of the marginalization idea (later briefly referred to as marg), which however creates new problems.

The information carried by the removed variable is passed on to the variables with which it is associated due to marginal probability, the information matrix is passed as shown below, where the variable to be removed is $\Lambda_{\beta\beta}$. i.e:

$$\Lambda = \Lambda_{\alpha\alpha} - \Lambda_{\alpha\beta}\Lambda_{\beta\beta}^{-1}\Lambda_{\beta\alpha} \tag{45}$$

For the marginalization process, it is assumed that marginalization is performed for ε_1. Before marg, the least-squares information matrix constructed for variable ε_1 and the corresponding measurement S_1 is denoted as $b_1(k), \Lambda_1(k)$. After marg, the new information matrix can be obtained from Eq. (44) as $b_p(k), \Lambda_p(k)$, respectively, where the subscript p is the prior, which is denoted as the a priori information on $\varepsilon_2, \varepsilon_3, \varepsilon_4, \varepsilon_5$. From $b_p(k), \Lambda_p(k)$ it is possible to solve the residual $r_p(k)$ and the Jacobi matrix $J_p(k)$, whereby the state of the window system before and after marg constitutes the residual, where $X = [x_c, x_p]$ is the set of bit poses and waypoints. This residual constitutes a cost function denoted as:

$$\| r_p - J_p X \|_{\Sigma_p}^2 \tag{46}$$

2.3. VIO-SLAM algorithm for EKF fusion of multidimensional dynamic data

In this paper, semantic segmentation and IMU are used to improve the estimation accuracy of the data, but the camera always has its limitations, thus in this paper, the Extended Kalman Filter (EKF) algorithm [29] is used to fuse the bit-position data to obtain more accurate results.

For the data fusion system in this paper, the nonlinear equation of motion is denoted as:

$$\hat{X}_k = f(\hat{X}_{k-1}, \hat{u}_{k-1}, w_{k-1}) \tag{47}$$

where $\hat{X}_{k-1}$ means $k-1$ moment estimate; $\hat{u}_{k-1}$ means $k-1$ moment control quantity; w_{k-1} means motion noise and conforms to Gaussian distribution $w_k - 1 \sim N(0, Q)$.

The position data acquired by the monocular camera/IMU (VIO) and the odometer are used as inputs and substituted into the observation equation of the EKF, which is denoted as:

$$Z_k = h(X_k, v_{k-1}) \tag{48}$$

where v_{k-1} is the observation noise for which the same Gaussian distribution assumption is made i.e. $v_{k-1} \sim N(0, R)$. Now linearize the equations of motion and the observation equations and since the system is not linearizable at the true point due to the presence of error in the system, $\hat{X}_{k-1}$ is chosen for the linearization denoted as:

$$X_k = f(\hat{X}_{k-1}, \hat{u}_{k-1}, w_{k-1}) + A(x_k - \hat{X}_{k-1}) + w_{kw,k-1} \tag{49}$$

Since w_{k-1} is unknown and a further simplification of Eq. (48) is required, assuming $w_k - 1 = 0$, let $f(\hat{X}_{k-1}, \hat{u}_{k-1}, 0) = \tilde{X}_k$. Denote A and $w_{kw,k-1}$ as:

$$\begin{cases} A = \dfrac{\partial f}{\partial x} | (\hat{X}_{k-1}, u_{k-1}) \\ w_{kw,k-1} = \dfrac{\partial f}{\partial w} | (\hat{X}_{k-1}, u_{k-1}) \end{cases} \tag{50}$$

At this point $w_{kw,k-1} \sim N(0, wQw^T)$, equation (49) is organized and recorded as the following equation:

$$X_k = \tilde{X}_k + A(x_k - \hat{X}_{k-1}) + w_{kw,k-1} \tag{51}$$

Similarly the observation equation can be linearized to obtain:

$$Z_k = h(\tilde{X}_k, v_k) + H(X_k - \tilde{X}_k) + V_{vk} \tag{52}$$

Let $v_k = 0$ be, then let the expressions $h(\tilde{X}_k, 0) = \tilde{Z}_k$, H and V_{vk} be:

$$\begin{cases} H = \dfrac{\partial h}{\partial x} | (\tilde{X}_k) \\ V_{vk} = \dfrac{\partial f}{\partial v} | (\tilde{X}_k) \end{cases} \tag{53}$$

At this point $V_{vk} \sim N(0, VRV^T)$, equation (52) is organized and recorded as the following equation:

$$Z_k = \tilde{Z}_k + H(X_k - \tilde{X}_k) + V_{vk} \tag{54}$$

This linearizes the nonlinear equations of motion and observation, at which point the data can be fused using the KF algorithm. The resulting prediction equation for the EKF is Eq. (55); the a priori estimated covariance is noted as Eq. (56):

$$\hat{X}_k^- = f(\tilde{X}_{k-1}, \tilde{u}_{k-1}, 0) \tag{55}$$

$$P_k^- = AP_{k-1}A^T + wQw^T \tag{56}$$

Combining Eq. (56) yields the Kalman gain K_k, denoted as:

$$K_k = \frac{P_k^- H^T}{HP_k^- H^T + VRV^T} \tag{57}$$

The final update phase is noted as:

$$X_k = \hat{X}_k^- + K_k[Z_k - h(\hat{X}_k^-, 0)] \tag{58}$$

$$P_k = (I - K_k H)P_k^- \tag{59}$$

The set of positional data acquired by the VIO and the odometer are fitted to the curve by the least squares method to obtain two nonlinear equations, which are used as the equations of motion and the observation equations in the EKF, respectively.

3. Effectiveness of the VIO-SLAM method in smart monitoring of seat belts

3.1. Model Performance Analysis

3.1.1. Experimental data set:

1) Grid construction dataset (GC): a large amount of data is required to learn the features within the classes by deep learning, but the bit-position dataset acquired by previous odometers can be limited in terms of various classes and the number of instances per class. Common grid construction environment categories are queried from the database, each containing no less than 15 object instances. Forty common object categories were selected to form the GC dataset, including 13,567 LSAM models.

2) Positional data set (PDOS) acquired by the odometer in the grid construction environment: the large semantic 3D data set contains 200 grid construction environments, and the positional data set acquired by the odometer includes six regions. The multi-dimensional dynamic data involved in intelligent monitoring of seat belts include “shoulder, leg, chest, neck, left thigh” and other stress areas. Finally, a category of clutter is added and each point in the scan is labeled using one of them. Of the two datasets, 80% were used for training and 20% for testing.

3.1.2. Analysis of the effect of model application. In the analysis of the effectiveness of the model application, the datasets used in this paper are GC and PDOS, which are the same as those used for real-time computational image classification of dynamic data, in which 2500 points are uniformly sampled on the grid surface and normalized to unit triangles. During training, the training volume of the point cloud data is increased by rotating the upper axis and dithering the points by Gaussian noise with zero mean and 0.005 standard deviation.

In this paper, the experimental environment is Ubuntu, the framework used is the same as GC and PDOS, the batch size of each experiment is 34, the number of input points is 2,000, the initialization of the learning rate is 0.001, the learning rate decay parameter is 0.85, and the step size is 1.5×10^5, and the loss function is optimized by using Adam optimizer.

PDOS exists five convolutional layers and one maximum pooling layer. Firstly, in order to test the effectiveness of BA, this paper tests the results of BA added at different positions, and the classification results of different BA positions are shown in Table 1. When testing the BA, the dataset used is GA, the settings are consistent with PDOS, and the number of input points is 1500. adding the corresponding BA after each convolutional layer, it can be seen that adding the BA after the first convolutional layer and the third convolutional layer, there is a relatively large improvement in the effect. It can be concluded that the BA proposed in this paper is effective, but it can also be concluded that the PDOS is sensitive to the location of the BA.

Table 1. Classification results of different BA module locations

Add position	Accuracy of point cloud	Average accuracy
PointNet	86.448	89.603
Convolution 1	87.659	90.256
Convolution 2	86.312	89.617
Convolution 3	87.143	89.875
Convolution 4	87.133	89.908
Convolution 5	96.931	89.299
Maximum pooling layer	87.435	89.481

The experimental results of 3D target classification under different methods are shown in Table 2. It can be seen that the model proposed in this paper is compared with previous work, and the benchmark PointNet. The method proposed in this paper achieves a better performance in the 3D input (volume and point cloud) based approach, when the average accuracy of the model in this paper and the point cloud accuracy reaches 98.572% and 97.767%, respectively, which are higher than the other models.

Table 2. Different methods of three-dimensional target classification results

Method	Input	Angle number	Average accuracy(%)	Accuracy of point cloud(%)
SPH	Grid	—	70.492	86.843
3DShapeNets	Body element	3	79.508	87.974
VoxNet	Body element	14	84.962	87.809
Subvolume	Body element	22	88.245	91.234
LFD	Picture	12	77.475	—
MVCNN	Picture	82	92.531	—
PointNet	Point cloud	—	85.714	89.216
PointNet (baseline)	Point cloud	—	87.527	90.661
Ours method	Point cloud	—	98.572	97.767

3.1.3. Analysis of Semantic Segmentation Results. In the segmentation experiments, the experimental data used is the PDOS dataset. In order to prepare the training data, the room is first segmented by room and divided into 1 meter x 1 meter regions, and the points within each chunked region are predicted using the segmentation network proposed in this paper. The batch size used in the experiments of this paper is 24, the learning rate is set to 0.001, the learning rate decay parameter is 0.5, the learning rate decay step is 2×10^5, and the Adam optimizer is used to optimize the loss function.

The PDOS dataset was divided into six regions using a six-fold cross-validation method, such that if region one is to be tested, the data from region two to region six are used as the training data, and if region two is to be tested, region one, region three to region six are used as the training data, and so on.

The results of the PDOS experiments are shown in Table 3. The results obtained from PointNet and this paper's method corresponding to the post-training test for each region are listed in the table, respectively. It can be seen that the IOU and accuracy of this paper's method on each model are improved compared to PointNet, and finally the average IOU of the six regions is higher than the baseline by roughly 36.08%, and the accuracy is improved by roughly 36.58%, which demonstrates that the method proposed in this paper is more accurate for intelligent monitoring of seat belts in grid construction environments, and that its method is feasible.

Table 3. PDOS experiment results

Test data	Measuring index	PointNet	Ours method
Zone 1	IOU	59.265	60.057
	Accuracy rate	86.955	86.58
Zone 2	IOU	35.013	37.47
	Accuracy rate	70.261	76.778
Zone 3	IOU	60.637	62.234
	Accuracy rate	89.643	89.024
Zone 4	IOU	46.047	45.861
	Accuracy rate	84.523	83.432
Zone 5	IOU	48.066	46.713
	Accuracy rate	86.098	83.629
Zone 6	IOU	71.013	71.34
	Accuracy rate	92.562	90.957
Mean value	IOU	54.3402	85.007
	Accuracy rate	53.9458	85.067

3.2. Practical case studies

This paper investigates the performance of intelligent monitoring harnesses for overhead construction in a grid construction environment.

3.2.1. Protection performance analysis. In order to compare and analyze the restraint protection effect of RPS on construction personnel, traditional RPS, traditional pre-tensioned safety belt (CPS) and smart monitoring safety belt (SMSB) were used to restrain and protect the construction personnel under the same emergency collision avoidance conditions in the power grid environment, and then simulation experiments were carried out.

1) Shoulder belt force analysis. Figure 3 shows the simulation results of the shoulder belt force part of the seat belt. The results show that during the emergency braking process, the shoulder belt force of SMSB integrates the advantages of CPS and RPS, i.e., at the beginning of braking (at 405ms), the shoulder belt binding force is linearly and gradually increased to about 370N by utilizing the function of RPS, at this time, the shoulder belt binding force is the pre-collision pretension, which is able to make full use of the advantageous time before the collision to eliminate the gap between the safety belt and the construction personnel, and to It can make full use of the favorable time before the collision to eliminate the gap between the seat belt and the construction personnel, and prevent the construction personnel from leaning forward and other sitting postures of excessive displacement.

At the moment of collision, the CPS function is utilized to rapidly increase the shoulder belt restraint force, which can instantly reach about 1585N, preventing the construction worker from leaning forward severely and colliding with the steering wheel. When the preload force reaches the threshold value of the force limiter, the SMSB webbing can be further released resulting in an instantaneous decrease of the shoulder belt force to 215N, after which the shoulder belt force gradually increases with the forward leaning of the worker's upper body. Therefore, during the collision avoidance process, both RPS and SMSB can reduce the forward leaning of the construction worker's body due to the inertia force during emergency braking, and improve the off-position sitting posture of the construction worker. However, at the moment of collision, the RPS lacks large enough restraint preload and the emergency braking takes about 112 ms, while the SMSB only takes 63 ms. It can be seen that the model in this paper not only has enough restraint force (4179 N), but also can restrain the construction personnel and construction equipment seats as one in the shortest time, which improves the restraint protection effect.

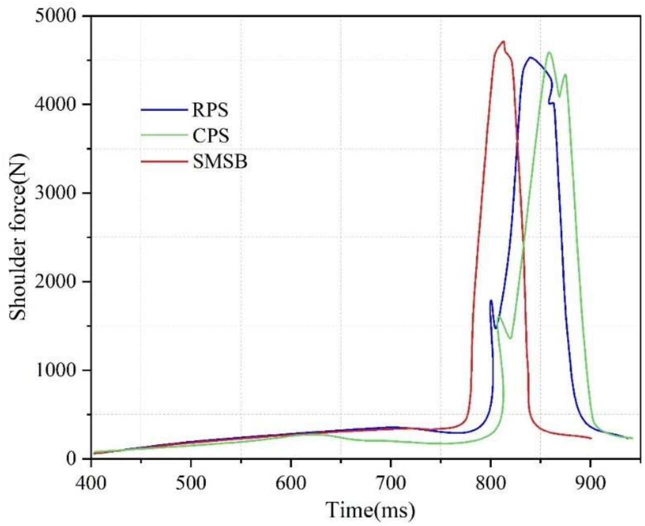

Fig. 3. The simulation results of the seat belt of the shoulder belt

2) Neck bending moment force analysis. Figure 4 shows the variation curves of neck bending moments under the protection of three types of safety belts. Under the protection of CPS, the maximum value of the construction worker's neck bending moment (My) appeared prematurely and with a large value between 820 ms and 860 ms. Under RPS protection, the peak neck bending moment of the construction worker appeared at 873 ms. With the SMSB, the peak neck bending moment of the worker appeared later (844 ms), and the force values were significantly smaller than those of the other two belts.

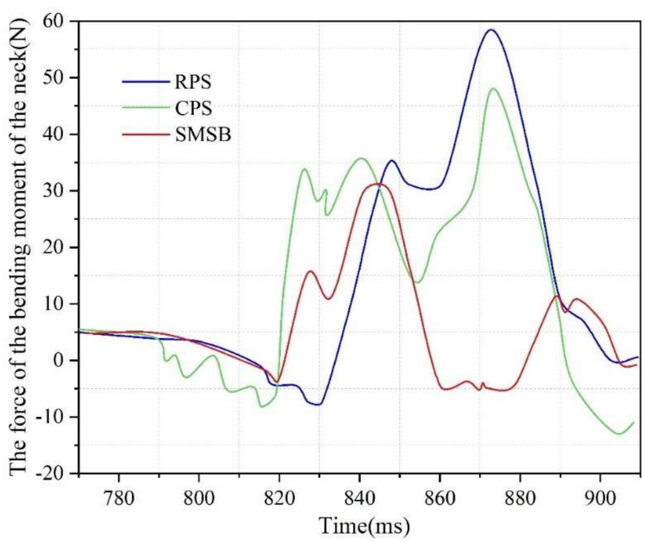

Fig. 4. The curve of the curve of the neck of the neck

3) Head acceleration analysis. Figure 5 shows the variation curve of head acceleration. Under the restraint protection of CPS, the head acceleration of the construction worker appeared peaked prematurely at 861ms, and then decreased rapidly, indicating that the head was in contact with the airbag. In the RPS restraint, although the peak head acceleration is slightly behind the CPS restraint, the peak is relatively large and it is not effective in pulling the worker back to the seatback. Under SMSB restraint protection, the head acceleration value of the construction worker is relatively flat and

the peak appears the latest (878ms), which is less likely to be hurt by the explosion of the airbag, and this also shows that SMSB has better protection effect.

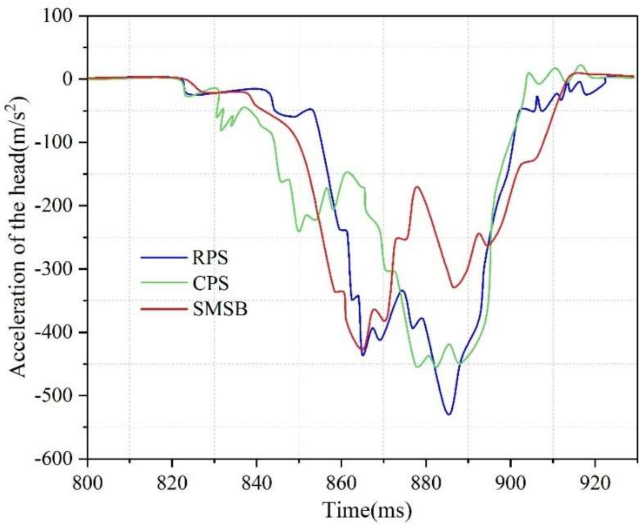

Fig. 5. The change curve of the head acceleration

3.2.2. Bench test study of preload performance. In order to investigate the preload speed at different pulse width modulation (PWM) duty cycles and the shoulder belt preload force at different control currents, bench experiments were carried out by mounting an active preload seat belt on a laboratory bench seat using the methodology of this paper. Before the experiment, volunteers and crash dummies were utilized to simulate the seating position of construction personnel, respectively. During the experiment, a high-speed camera and a shoulder belt force sensor were used to collect the corresponding experimental data. The experimental results of the preload performance are shown in Fig. 6, (a) and (b) are the shoulder belt preload force under different control currents and the preload speed under different pulse-width modulation duty cycles, respectively.

From Fig. (a), it can be seen that the preload force has a positive relationship with the size of the control current, i.e., as the control current increases the shoulder belt preload force increases accordingly. The minimum current that can make the intelligent monitoring seat belt start working is 10A; where the control current is 50A, the maximum value of the shoulder belt force is about 463.2N, and the preload force can satisfy the first level of preload constraints before the collision. A greater restraint force is required if the vehicle is involved in a collision.

From Fig. (b), it can be seen that the preload speed has a positive correlation with the PWM duty cycle, and the larger the PWM duty cycle is, the larger the preload speed is. The average preload speed in the first 250ms is 0.0962 m/s to 0.3978 m/s, and the average preload speed in the whole process is 0.0837 m/s to 0.3641 m/s. This preload speed can effectively eliminate the amount of slack between the webbing and the constructor.

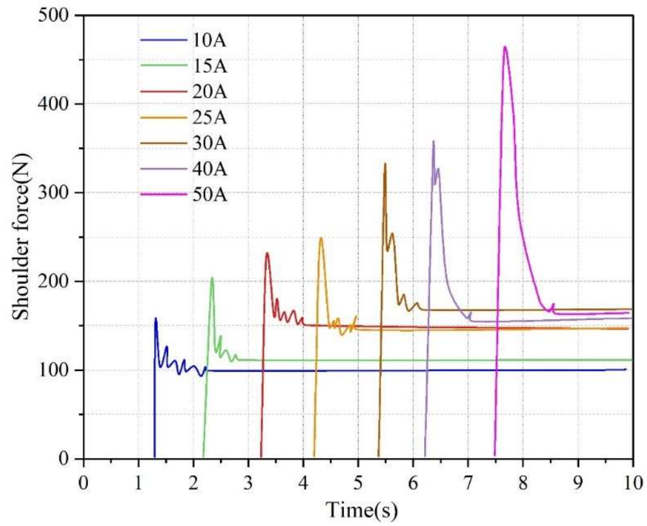

(a)The shoulder belt is pretight under different control currents

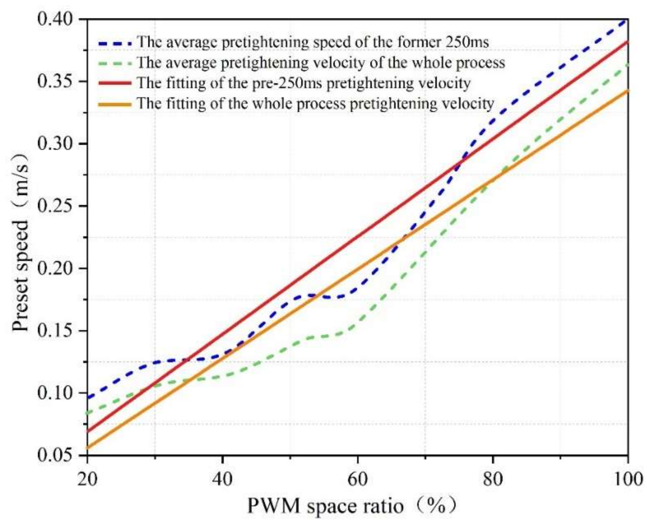

(b)Different pulse width modulation is the pre-tight speed of the empty ratio

Fig. 6. Experimental results of pre-compacting properties

3.2.3. Experiments on preloading performance in real vehicles. In order to determine the proper seatbelt preload to eliminate the amount of webbing gap during crash avoidance, an actual volunteer grid construction operations experiment was conducted. Prior to the start of the experiment, 15 male and 15 female volunteer constructors were selected, and the height and weight of the volunteer constructors were basically spread across the range of common constructor physical characteristics. During the experiment, the height and weight of each volunteer and their subjective perception of the more appropriate preload force were recorded. Figure 7 shows the distribution of the preload force that the volunteers subjectively felt was appropriate for eliminating the webbing gap; Figure 8 shows the distribution of the minimum preload force that the volunteers felt was uncomfortable at the time of the experiment; (a) ~ (b) represent height and body mass, respectively.

From the results, it can be seen that the preload range of male and female volunteers for the subjective feeling of eliminating the webbing gap was 39.33N-68.93N and 38.57N-54.59, respectively, but the mean value of their preload for eliminating the webbing gap did not show a significant difference between the genders, and the minimum preloads for males and females were 52.03N and 47.21N, respectively.The minimum preloads for the testing of the uncomfortable feeling in the In the test of the minimum preload force when feeling uncomfortable, the values of the minimum preload force showed some differences between genders, in which the mean value of the minimum preload force when feeling uncomfortable was 169.17N for the male volunteers and 160.39N for the female volunteers, with a difference of 8.78N. It can be seen that the volunteers' subjective preload force showed a significant difference in terms of the differences in height and weight. The differences showed significant variability. In practical application, the average value of all the statistical data can be used as the initial setting value of the intelligent monitoring seat belt in the power grid construction environment.

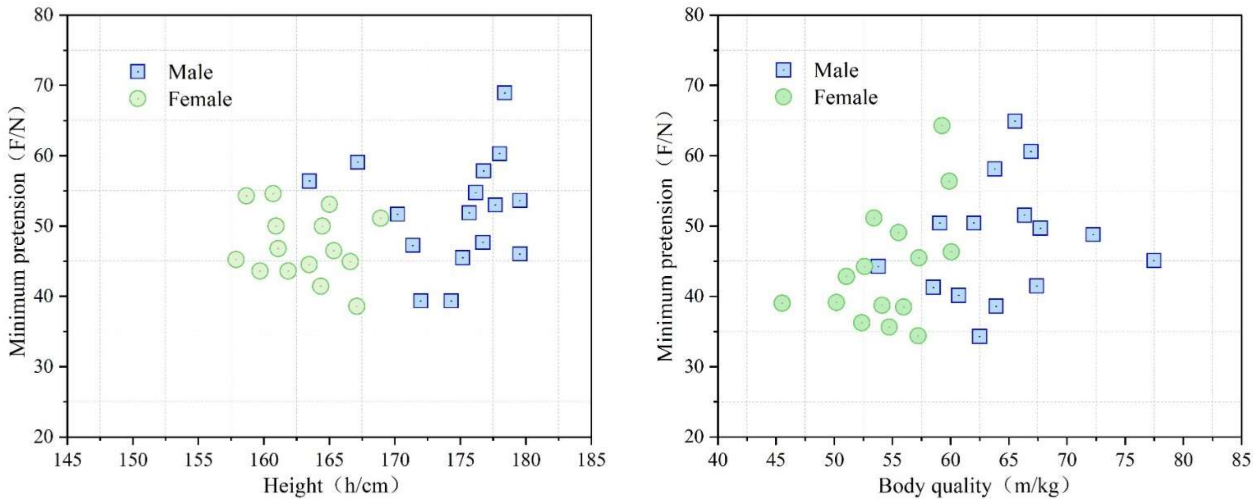

(a)Height (b)Weight

Fig. 7. The pre-tight force distribution of subjective feelings

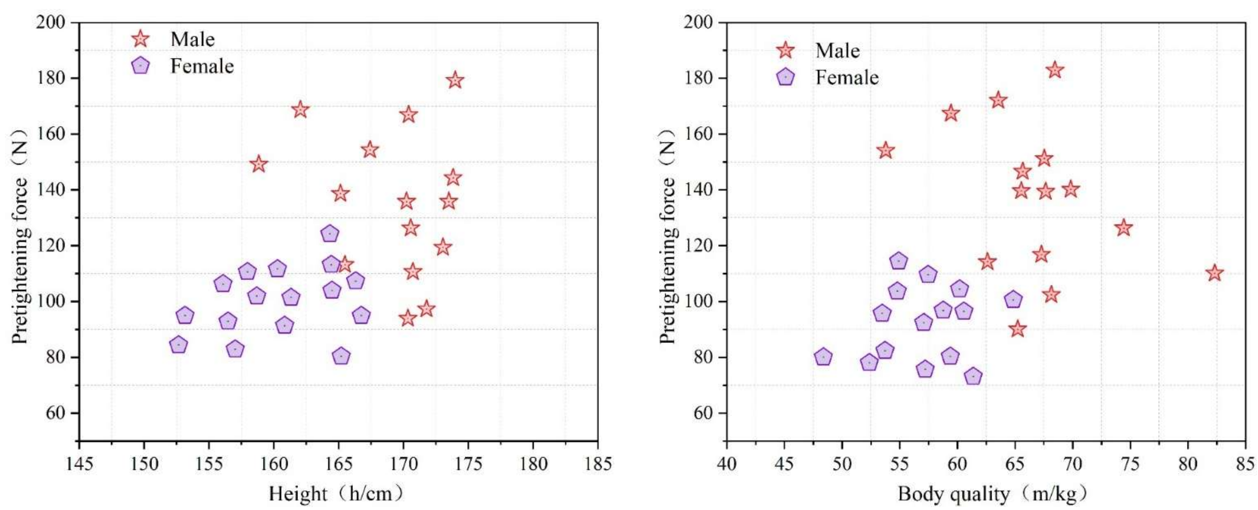

(a)Height (b)Weight

Fig. 8. The minimum pre-tightening force distribution of the feeling of discomfort

4. Conclusion

This paper focuses on the multi-dimensional data dynamic fusion and real-time computation method for intelligent monitoring of safety belts, and proposes a monitoring system that synthesizes point and line data processing algorithms, inertial measurement units (IMUs) and semantic information. It also combines the EKF fusion algorithm to fuse the complex multidimensional dynamic data in the power grid construction environment, and explores the protection effect of the intelligent monitoring seat belt on construction personnel under the method of this paper. The results show that:

1) The average accuracy (98.572%) and point cloud accuracy (97.767%) of the method proposed in this paper are higher than other models among 3D input methods. The accuracy of this paper's method is higher for intelligent monitoring of seat belts in the grid construction environment, and its IOU and accuracy are 36.08% and 36.58% higher than that of the PointNet baseline model.

2) The intelligent monitoring safety belt under the method of this paper can tighten the safety belt in advance in the process of emergency collision avoidance to protect the construction personnel and achieve the purpose of "collision avoidance and damage reduction". The bench experiment tested the pre-tensioning speed and shoulder belt pre-tensioning force of the intelligent monitoring seat belt, and found that the average pre-tensioning speed of the whole pre-tensioning process was between 0.0837 m/s and 0.3641 m/s, and the maximum value of the shoulder belt force at this time was within 463.2 N. The results of the real vehicle experiment determined that the elimination of seat belt pre-tensioning could be achieved during the emergency collision avoidance process. The results of the real-vehicle experiments determined the preload force for eliminating the seat belt webbing gap, clarified the preload force for the somatosensory warning reminder, and realized the function of somatosensory warning reminder in the process of emergency collision avoidance.

Funding

This research was Supported by China Southern Power Grid Corporation [(project number: 035100KC23040005 (GDKJXM20230317)].

References

[1] Oliveira, B. A. S., Neto, A. P. D. F., Fernandino, R. M. A., Carvalho, R. F., Fernandes, A. L., & Guimaraes, F. G. (2021). Automated monitoring of construction sites of electric power substations using deep learning. IEEE Access, 9, 19195-19207.

[2] Lu, J., Yu, W., & Wu, S. (2024). Automatic monitoring and early warning method for power grid infrastructure investment progress using building information model and blockchain. IET Blockchain, 4, 494-506.

[3] Chen, Q., Li, Q., Wu, J., He, J., Mao, C., Li, Z., & Yang, B. (2023). State monitoring and fault diagnosis of HVDC system via KNN algorithm with knowledge graph: a practical China power grid case. Sustainability, 15(4), 3717.

[4] Pan, Y., Zhu, M., Lv, Y., Yang, Y., Liang, Y., Yin, R., ... & Yuan, X. (2023). Building energy simulation and its application for building performance optimization: A review of methods, tools, and case studies. Advances in Applied Energy, 10, 100135.

[5] Zhang, J., Xuan, X., Xu, Z., & Shao, X. (2020). The Distribution Network Operation Online Monitoring and Analysis System of State Grid Corporation (Phase 5). In IOP Conference Series: Materials Science and Engineering (Vol. 719, No. 1, p. 012013). IOP Publishing.

[6] del Amo, A., Martínez-Gracia, A., Bayod-Rújula, A. A., & Antoñanzas, J. (2017). An innovative urban energy system constituted by a photovoltaic/thermal hybrid solar installation: Design, simulation and monitoring. Applied Energy, 186, 140-151.

[7] Wan, Z., Li, J., & Gao, Y. (2018). Monitoring and diagnosis process of abnormal consumption on smart power grid. Neural Computing and Applications, 30, 21-28.

[8] Lee, D., Cha, G., & Park, S. (2016). A study on data visualization of embedded sensors for building energy monitoring using BIM. International journal of precision engineering and manufacturing, 17, 807-814.

[9] Zhang, C., Liu, Q., Chen, B., Huang, Z., Huang, X., & Yan, Y. (2023, March). Research and Practice on Slope Monitoring of Power Grid Construction Based on IoT Technology. In Journal of Physics: Conference Series (Vol. 2452, No. 1, p. 012018). IOP Publishing.

[10] Oliveira, B. A. S., Neto, A. P. D. F., Fernandino, R. M. A., Carvalho, R. F., Fernandes, A. L., & Guimaraes, F. G. (2021). Automated monitoring of construction sites of electric power substations using deep learning. IEEE Access, 9, 19195-19207.

[11] Wu, J. (2023). Design and Exploration of Real Time Monitoring System for Power Grid Operation Safety Based on YOLO Object Detection Algorithm. Procedia Computer Science, 228, 889-897.

[12] Zhang, C., Zhang, L., Chen, X., Ou, L., & Xu, Y. (2024). Octree based visual monitoring method for operation process of power construction site. Results in Engineering, 24, 103138.

[13] Liu, Z., Tan, Q., Zhou, Y., & Xu, H. (2021). Syncretic application of IBAS-BP algorithm for monitoring equipment online in power system. IEEE access, 9, 21769-21776.

[14] Gao, Q., Han, Y., Yang, J., Zhang, G., Hong, Y., Ding, C., & Cao, W. (2021). Research on Dynamic Monitoring and Early Warning Model of Fund for Power Grid Infrastructure Projects. In E3S Web of Conferences (Vol. 245, p. 01059). EDP Sciences.

[15] Flôr, V. B. B., Do Coutto Filho, M. B., de Souza, J. C. S., & Ochi, L. S. (2022). Strategic observation of power grids for reliable monitoring. International Journal of Electrical Power & Energy Systems, 138, 107959.

[16] Mufana, M. W., & Ibrahim, A. (2022). Monitoring with communication technologies of the smart grid. IDOSR Journal of Applied Sciences, 7(1), 102-112.

[17] Jiang, J. A., Wang, J. C., Wu, H. S., Lee, C. H., Chou, C. Y., Wu, L. C., & Yang, Y. C. (2020). A novel sensor placement strategy for an IoT-based power grid monitoring system. IEEE Internet of Things Journal, 7(8), 7773-7782.

[18] Rong, J., Su, Y., Zhou, Y., & Li, L. (2023, May). Application Research of Online Monitoring Technology for Smart Low-Carbon Power Grid Construction. In 2023 6th International Conference on Energy, Electrical and Power Engineering (CEEPE) (pp. 449-453). IEEE.

[19] Shin, H., Song, Y., & Kong, P. Y. (2021). Robust online overhead transmission line monitoring with cost efficiency in smart power grid. IEEE Access, 9, 86449-86459.

[20] Zhang, Z., Han, W., Rong, J., Liu, H., & Ma, W. (2024, June). Construction monitoring of power grid engineering based on UAV remote sensing images. In 2024 2nd International Conference on Mechatronics, IoT and Industrial Informatics (ICMIII) (pp. 424-428). IEEE.

[21] Jiang, J. A., Chiu, H. C., Yang, Y. C., Wang, J. C., Lee, C. H., & Chou, C. Y. (2022). On real-time detection of line sags in overhead power grids using an iot-based monitoring system: theoretical basis, system implementation, and long-term field verification. IEEE Internet of Things Journal, 9(15), 13096-13112.

[22] Li, S., & Li, J. (2017). Condition monitoring and diagnosis of power equipment: review and prospective. High Voltage, 2(2), 82-91.

[23] Li, B., Wang, W., Guo, J., & Ding, B. (2024). Research on condition operation monitoring of power system based on supervisory control and data acquisition model. Alexandria Engineering Journal, 99, 326-334.

[24] Babatunde, O. M., Munda, J. L., & Hamam, Y. (2022). Off-grid hybrid photovoltaic–micro wind turbine renewable energy system with hydrogen and battery storage: Effects of sun tracking technologies. Energy Conversion and Management, 255, 115335.

[25] Muqing Deng,Yi Zou,Zhi Zeng,Yanjiao Wang,Xiaoreng Feng & Yuan Liu. (2025). Human gait recognition based on frontal-view sequence using discriminative optical flow feature representations and learning. Engineering Applications of Artificial Intelligence110213-110213.

[26] Jan Březina & Pavel Exner. (2017). Fast algorithms for intersection of non-matching grids using Plücker coordinates. Computers and Mathematics with Applications(1),174-187.

[27] Wenlan Ouyang,Wanbiao Lin & Lei Sun. (2025). A dynamic and static combined camera-IMU extrinsic calibration method based on continuous-time trajectory estimation. Robotics and Autonomous Systems104916-104916.

[28] Jie Zhong,Aiguo Chen,Yizhang Jiang,Chengcheng Sun & Yuheng Peng. (2025). Lightweight and efficient feature fusion real-time semantic segmentation network. Image and Vision Computing105408-105408.

[29] Shuxin Zhong,Li Cheng,Haiwen Yuan & Xuan Li. (2025). Adaptive Kalman Filter Fusion Positioning Based on Wi-Fi and Vision. Sensors(3),671-671.